

Process and nozzle design for high-resolution dry aerosol direct writing (dADW) of sub-100 nm nanoparticles

Aghajani, Saleh; Accardo, Angelo; Tichem, Marcel

DOI

[10.1016/j.addma.2022.102729](https://doi.org/10.1016/j.addma.2022.102729)

Publication date

2022

Document Version

Final published version

Published in

Additive Manufacturing

Citation (APA)

Aghajani, S., Accardo, A., & Tichem, M. (2022). Process and nozzle design for high-resolution dry aerosol direct writing (dADW) of sub-100 nm nanoparticles. *Additive Manufacturing*, 54, Article 102729. <https://doi.org/10.1016/j.addma.2022.102729>

Important note

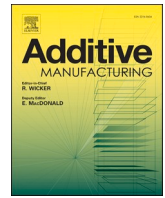
To cite this publication, please use the final published version (if applicable). Please check the document version above.

Copyright

Other than for strictly personal use, it is not permitted to download, forward or distribute the text or part of it, without the consent of the author(s) and/or copyright holder(s), unless the work is under an open content license such as Creative Commons.

Takedown policy

Please contact us and provide details if you believe this document breaches copyrights. We will remove access to the work immediately and investigate your claim.



Research paper

Process and nozzle design for high-resolution dry aerosol direct writing (dADW) of sub-100 nm nanoparticles

Saleh Aghajani^{*}, Angelo Accardo, Marcel Tichem

Delft University of Technology, Faculty of Mechanical, Maritime, and Materials Engineering (3ME), Department of Precision and Microsystems Engineering (PME), Mekelweg 2, Delft 2628 CD, The Netherlands

ARTICLE INFO

Keywords:

Nanoparticle
Direct writing
Dry aerosol direct-writing
Aerodynamic focusing
Sheath gas nozzle

ABSTRACT

One of the essential requirements to create nanoparticle (NP)-based applications and functions is the ability to control their deposition in specific locations. Many methods have been proposed, with wet direct writing (DW) techniques such as inkjet printing being the most employed. These methods generally depend on off-line and solvent-based NP synthesis leading to contamination and impurity in the final NP film as well as inhomogeneity in the deposition caused by solution-substrate interactions. This paper introduces a dry aerosol direct writing (dADW) method, which combines spark ablation-based and solvent-free NP synthesis with spatially selective deposition using aerodynamic focusing in a vacuum chamber. The challenge is to print high-resolution lines and spots of nanoparticles with a diameter < 100 nm. We study two aerodynamic nozzle concepts, a converging nozzle (CN) and a sheath gas nozzle (SGN), and investigate numerically how their design, as well as operating parameters, relate to the deposition process performance. This is quantified by three criteria: contraction factor, focusing ratio, and collection efficiency. We also compared our numerical results to experimental assays by manufacturing two SGNs and three CNs and evaluating the performance of each nozzle in terms of resolution, sharpness and thickness of the line. Using one of the SGN designs with an outlet diameter of $248 \mu\text{m}$ and an aerosol to total flow rate ratio of 0.17, we achieved a high-resolution line with a width of $67 \mu\text{m}$, i.e., equal to 27% of the nozzle diameter, when printing < 100 nm Au NPs. The presented additive manufacturing method enables, therefore, the creation of high-resolution and sharp patterns of metallic nanoparticles, which can be employed in a wide range of applications, ranging from interconnects to optical and gas sensors.

1. Introduction

Nanoparticles (NPs) are the foundation of many devices and applications with complex properties and functionalities [1–6]. This includes optical coatings [7], catalysis [6], biosensors [8,9], electrical interconnects [10] and many more. As a result, NP manipulation is required for a wide range of scientific and industrial applications. Localised NP patterning, in particular, has received considerable attention in many studies due to its flexibility and compatibility, including microelectronics [11,12], optics [13–15] and sensing [16,17]. Several techniques have been proposed to enable localised NP deposition, with direct writing (DW) methods being one of the most prominent. Nanoparticle direct writing is a class of additive manufacturing techniques that uses a controlled deposition of nanoparticles to produce patterns and features on the surface without the need for lithography processes. Techniques such as inkjet printing (IJP) [18–21] and

aerosol-jet printing (AJP) [22–26] are widely-used examples of nanoparticle DW deposition techniques. In both methods, droplets of liquid containing nanoparticles stabilised by surfactants [25,27] are deposited on the substrate [19,23] to create desired patterns. However, the use of chemical agents in the synthesis of NPs and for stabilisation of the suspension during printing may lead to contamination and affect the properties of the NP film.

In contrast to solvent-based NP deposition methods, in dry techniques, no chemical agents are present during particle synthesis and deposition, which reduces the possibility of particle contamination and impurity. Methods such as cold spray [28,29], Aerosol deposition [30], and Aerodynamically Focused Nanoparticle (AFN) [16,31] have been used for dry particle deposition. Methods such as cold spray and aerosol deposition, on the other hand, are used primarily for microparticles and do not take into account the focusing of particles on the substrate, while other approaches, such as AFN, rely on off-line particle synthesis.

In our previous work [8,32], we used a dry Aerosol Direct Writing

^{*} Corresponding author.

E-mail address: S.aghajani@tudelft.nl (S. Aghajani).

<https://doi.org/10.1016/j.addma.2022.102729>

Received 6 December 2021; Received in revised form 17 February 2022; Accepted 2 March 2022

Available online 4 March 2022

2214-8604/© 2022 The Author(s). Published by Elsevier B.V. This is an open access article under the CC BY license (<http://creativecommons.org/licenses/by/4.0/>).

Nomenclature		DW	Direct Writing
AFN	Aerodynamically focused nanoparticle	dADW	dry aerosol direct writing
AJP	AerosolJet printing	FR	Focusing ratio
AL	Aerodynamic lenses	IJP	Inkjet printing
AuNPs	Gold nanoparticles	L/D	Distance between nozzle to substrate/Diameter of nozzle
a/T	Volumetric flow rate of aerosol nozzle/total volumetric flow rate	NP	Nanoparticle
CE	Collection efficiency	RANS	Reynolds-averaged Navier–Stokes
CDN	Converging-diverging nozzle	SAM	Spark ablation method
CDCN	Converging-diverging-converging nozzle	SEM	Scanning electron microscopy
CF	Contraction factor	SGN	Sheath-gas nozzle
CN	Converging nozzle	TLD	Through-the-lens detector
		WD	Working distance
		WLI	White light interferometry

(dADW) technique to selectively generate patterns of NPs on substrates. In our method, particles are generated in-line using a spark ablation process [33]. They are subsequently transported using an inert gas (Ar) to a vacuum chamber for deposition immediately after formation as primary particles and agglomerates of primary particles. Spark ablation can produce extremely small primary particles with a size distribution in the 20 nm range and smaller [34,35]. The focused deposition of these nanoparticles, i.e., those with an aerodynamic diameter of less than 100 nm, is challenging due to their low inertia and tendency to follow streamlines through which they leave the deposition chamber without being deposited. There are several strategies for focusing particles, including aerodynamic [31,36–40], electrostatic [41], and electro/thermo-phoretic [42,43] focusing. Given the working principle of dADW, and due to the charge neutrality of NPs, the electrostatic and electro/thermophoresis focusing methods are not optimal for particle focusing in dADW. On the other hand, because of the presence of carrier gas and the simple operating concept of aerodynamic focusing nozzles, this method surpasses others. Various aerodynamic focusing nozzles have been proposed as aerosol collimation strategies, constraining the aerosol flow based on: 1) variation of nozzle cross-sections to increase the particle velocity and to collimate the particle beam, such as

converging nozzle (CN) [44], converging-diverging nozzle (CDN) [8], converging-diverging-converging nozzle (CDCN) [32], and aerodynamic lenses (AL) [8,40]; or 2) introduction of a sheath gas flow and leading to a sheath gas nozzle (SGN) [45] (Fig. 1). Based on the aerosol physics of a particle travelling through a gas medium (See [Supplementary Information-Section 1](#)) and the working principle of various aerodynamic focusing nozzles (discussed in [Supplementary Information-Section 1.2](#)), sheath gas nozzles outperform the other aerodynamic nozzle systems. They are less sensitive to the size of particles in contrast to CDCN and AL, the confinement of the aerosol flow in the centric region of the nozzle leads to a more uniform and higher velocity for NPs, and the sheath-gas flow, acting as a moving wall surrounding the aerosol flow, reduces defocusing of the aerosol flow also after leaving the nozzle. AJP employs a similar approach for focusing droplets; however, SGN in AJP operates at ambient pressure and in a subsonic flow regime, and droplets have sizes $> 1 \mu\text{m}$ [22,26,46].

The purpose of this paper is to deepen the knowledge, evaluate and validate the performance of the sheath-gas nozzle (SGN) for the additive manufacturing of fine nanoparticles (below 100 nm) and compare it to the conventional converging nozzle (CN) through numerical and empirical approaches. We identified the critical nozzle design

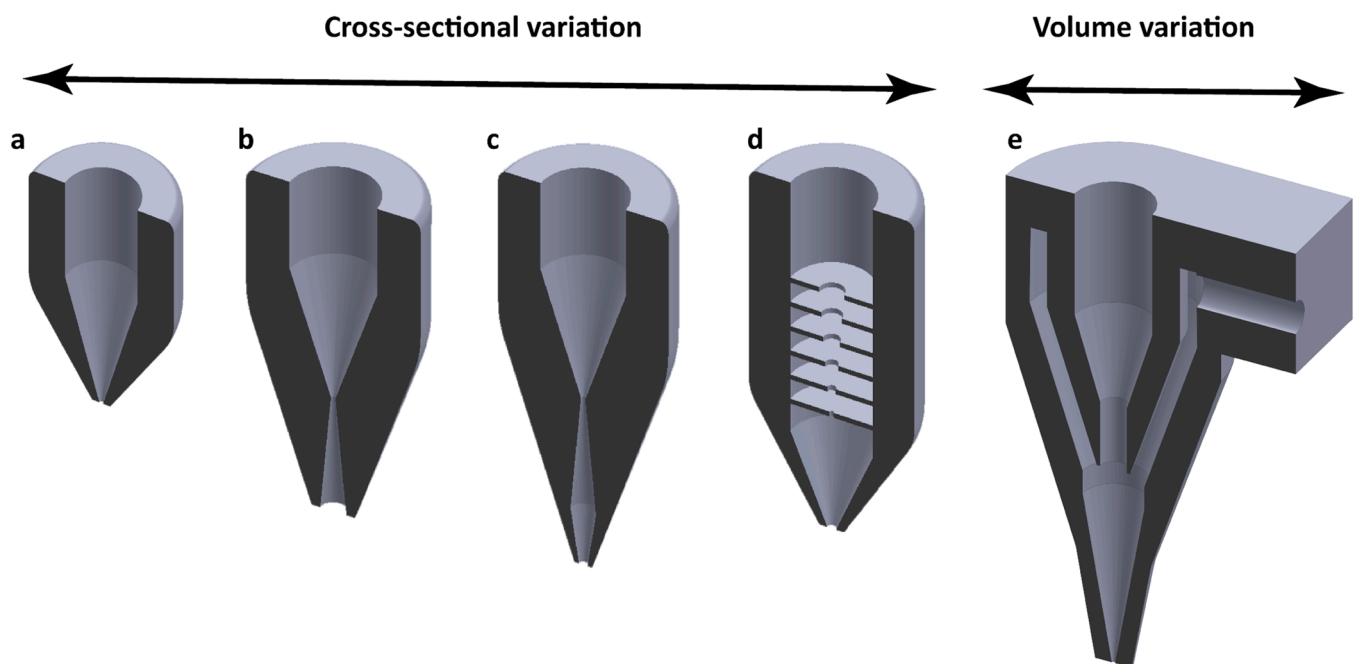


Fig. 1. Aerodynamic focusing nozzles: a) converging nozzle, b) converging-diverging nozzle, c) converging-diverging-converging nozzle, d) aerodynamic lenses, and e) sheath-gas nozzle.

parameters and the operating process parameters resulting in narrow lines for both types of nozzles, including half-angle of converging section, nozzle outlet radius, inner aerosol radius for SGN, downstream pressure, working distance and aerosol to total flow rate ratio for SGN. In order to support this analysis, we created finite element models in COMSOL Multiphysics [47] and related the design and process parameters to three figures of merit: the contraction factor, the focusing ratio, and the collection efficiency. Finally, we 3D printed two SGNs and three CNs and carried out experiments to evaluate the performance of each nozzle in terms of sharpness, resolution, and thickness. The morphology of lines in different parts of lines printed with both SGN and CN were investigated. The best result was a line with a width of 67 μm obtained with an SGN with an outlet diameter of 248 μm and aerosol to total flow rate ratio of 0.17.

2. Material and methods

2.1. Finite element modelling

We used COMSOL Multiphysics 5.5 to create finite element models that relate nozzle design and operating parameters to the deposition line width. This is accomplished in two steps. First, the gas flow profile throughout the system is determined, which includes the inlet(s), nozzle, and impaction plate placed in a vacuum chamber. Secondly, particles are introduced into the inlet at discrete radial entrance positions, and particle trajectories are computed. The stationary Reynolds-averaged Navier–Stokes (RANS) equations are used to determine the flow field in combination with a $k\text{-}\epsilon$ model to describe the turbulence. Sutherland's law is used to determine the dynamic viscosity and gas conductivity (See [Supplementary information: Section 2](#)).

Because of the symmetry of the system around the axial line of the nozzle, an axisymmetric 2D simulation, as shown in [Fig. 2.a](#) is used to reduce the computational cost of the simulation. A general design of a sheath gas and deposition systems system is depicted in [Fig. 2.a](#). The two up-stream boundaries are defined in COMSOL as an aerosol and sheath gas inlet with: a characteristic-based flow condition, a defined averaged gas flow velocity in the form of Mach number, a pressure (P_u) of 1 bar and a temperature of 293 K. The outlet pressure is defined as downstream pressure (P_d) with hybrid flow conditions. The boundary conditions that are applied to other walls are regarded as non-slip. The variable design parameters are the nozzle throat (exit diameter), the half-angle of the converging section, and the diameter of the aerosol nozzle when it meets the sheath gas. The variable process parameters are the working distance (distance between the nozzle throat and the impaction plate), the ratio of aerosol gas flow to total flow, and the downstream pressure. [Table 1](#) summarises the parameter value ranges

Table 1

Parameters and value ranges considered in the modelling.

	Design parameters		Operating parameters			
Converging nozzle	Half-angle (θ°)	1, 2.5, 5, 10, 15, 30	Working distance (μm)	200, 300, 400, 600, 800, 1000, 1200		
		Nozzle throat diameter (μm)		400, 600, 800	Downstream pressure P_d (Pa)	10, 100, 500, 1000, 2000, 5000
Sheath gas nozzle	Half-angle (θ°)	1, 2.5, 5, 10, 15, 30	Working distance (μm)	200, 300, 400, 600, 800, 1000, 1200		
		Radius of aerosol nozzle (mm)		1, 1.5, 2, 3	Downstream pressure P_d (Pa)	10, 100, 500, 1000, 2000, 5000
		The ratio of aerosol flow rate to the total flow rate		2/8, 3/8, 4/8, 5/8, 6/8, 7/8		

that were tested for both CNs and SGNs. As for the particles, a number of discrete diameter values of 5, 10, 20, 50, and 100 nm are tested. The trajectory of particles is calculated for gold with a density of 19300 kg/m^3 . The boundary condition in the FE model for the axial symmetry line is pass-through, allowing particles to cross the boundary unrestrained. The model assumes that after a particle reaches the impaction plate, it 'freezes' and sticks to the surface at that position.

To overcome the convergence problem in the flow profile calculation caused by the high-pressure ratio between the upstream and downstream position in the nozzle, the calculation is run for a coarse mesh and with a stepwise increase of upstream pressure, as shown in [Fig. 2.b](#) until it reaches 1 bar. The second step improves the modelling using this flow field as an initial value for the second calculation with two levels of adaptive mesh refinement. The adaptive mesh refinement takes the previous mesh and refines it in areas where it is needed, such as around the bow shock, to achieve a highly accurate flow regime in that position ([Fig. 2.c](#)).

These flow fields are then used to calculate particle trajectories by assuming a one-way interaction of particles in the flow, as the particle concentration is low and has no effect on the flow field ([Fig. 2.d](#)). The particles enter the aerosol inlet at the same velocity as the flow and are distributed uniformly along the radius. The Stokes drag force is the primary force acting on a particle in this system (as explained in [Supplementary Information: Section 1](#)), with extra time steps for wall interactions and rarefaction effects for the Cunningham slip correction factor explained in the [Supplementary Information: Section 1](#). The modelling results of the trajectory include the particle position on the

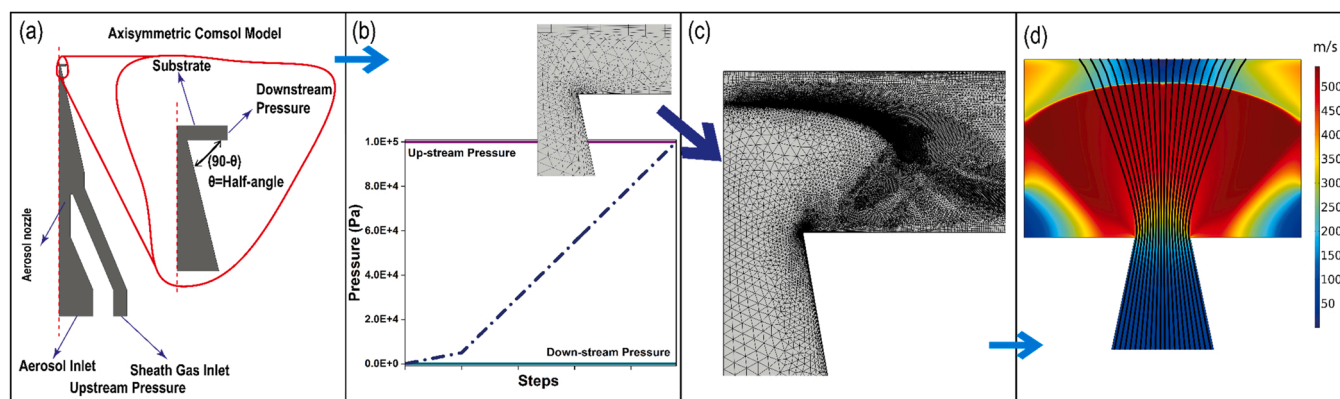


Fig. 2. Steps of COMSOL simulation, a) axisymmetric geometry considering inlet of aerosol and sheath gas, and impaction plate, b) course mesh for initial rough flow calculation with stepwise increase of inlet pressure, c) accurate simulation of the flow using adaptive mesh refinement and d) calculation of particle trajectory using the accurate flow simulation results.

impaction plate (if deposited). The radial and axial velocity of a particle along its path are then used in MATLAB for data process and visualisation.

2.2. Dry aerosol direct writing (dADW)

We use an experimental setup consisting of a commercial particle generator (VSParticle G1) and a vacuum deposition chamber for nozzle performance studies (Section 3: Fig. S2). The VSParticle G1 generates polydispersed metallic nanoparticles (Au) via a spark ablation method (SAM) from 99.99% pure gold electrodes. In this study, the SAM voltage and current are set to $V = 1.1$ kV and $I = 8$ mA, respectively, resulting in a stable particle generation process. The nanoparticles are carried using a pure argon flow and introduced into the nozzle system and the deposition chamber. Both converging and sheath gas nozzles are designed in SolidWorks (Fig. 3.a) and 3D printed using "3DM Tough" and a digital light projection Envisontec Micro Plus Hires setup. After printing and chemical removing the unexposed regions via sonication for 5 min in an IPA bath, the nozzles were UV cured for 6 min to improve the mechanical properties. To ensure a leak-free connection of the nozzles to the aerosol stream, the aerosol inlet of the nozzles is printed with a smaller diameter and mechanically drilled to 10 mm diameter for precise fitting. The nozzle's sheath gas inlet is drilled to an M5 hole and threaded to connect to a stainless-steel joint and clean argon gas (Fig. 3. b). Two nozzles with converging half-angles of 10° and actual outlet diameters of 484 and 248 μm are manufactured for the experimental investigation of the sheath gas nozzle. Three nozzles with manufactured outlet diameters of 166.5, 238.0, and 339.0 μm were used for the converging nozzle. Silicon substrates were used for deposition, which were first cleaned with acetone and isopropanol and then placed in an oxygen plasma chamber for 30 min before printing to remove any impurities from the substrate. The clean substrate is mounted on a holder perpendicular to the nozzle's central axis in the vacuum chamber. A SmarAct SLC-1750-O20-D-HV precision positioner controls the distance between the nozzle and the substrate. Using the in-plane SLC-1750-M-E-HV positioner, patterns were created by moving the stage relative to the nozzle. The nozzle's upstream pressure (P_u) is always set to 1 bar at room temperature, and the vacuum pressure (P_d) varies for each nozzle.

2.3. White-light interferometry

White-light interferometry with a Contour GT-K 3D optical profilometer (Bruker Corporation, Billerica, MA, USA) and integration of three measurements for each line were used to determine line width and thickness. The white-light interferometry data were post-processed in MATLAB to remove the background and calculate the thickness and width of the line at 640 cross-sections for the entire length of the line. Because of the Gaussian profile in the cross-section [19], the reported thickness is defined as the average thickness along the cross-section, as

shown in the [Supplementary Information: Section 4-Fig. S3](#).

2.4. Morphology characterisation

SEM measurements were carried out with a field-emission high-resolution Helios G4 setup detecting secondary electrons through-the-lens detector (TLD). Optical images were captured using a Keyence digital microscope (VHX-6000) with a magnification range of $20\times$ to $2000\times$. The HDR (high dynamic range) function improved the resolution and contrast between substrate regions with and without deposited AuNPs by allowing the capture of multiple images at varying shutter speeds. The boundary of the line was chosen as the region where there was a clear difference in the contrast.

3. Results and discussion

3.1. Numerical results

The simulation results for both converging and sheath gas nozzles are presented in this section. To express the performance of the deposition processes, we use three main figures of merit: the contraction factor (CF), the focusing ratio (FR), and the collection efficiency (CE). The contraction factor (CF) indicates particle collimation within the nozzle system and is defined based on the particle's radial position relative to the local nozzle radius at the entrance and exit of the nozzle, respectively:

$$CF = \frac{R_{i-\text{Inlet}} / \text{Radius}_{\text{Inlet}}}{R_{i-\text{Throat}} / \text{Radius}_{\text{Throat}}} \quad (1)$$

$R_{i-\text{Inlet}}$ and $R_{i-\text{Throat}}$ are the radial position of the i -th particle in the inlet and nozzle throat, respectively, while $\text{Radius}_{\text{Inlet}}$ and $\text{Radius}_{\text{Throat}}$ are inlet radius and nozzle throat radius, respectively. A $CF > 1$ indicates that particles are effectively pushed towards the central axis, beyond the effect expected from a decrease in nozzle diameter. The focusing ratio (FR) is defined as the line width (or deposition spot size diameter) divided by the nozzle throat diameter. $FR < 1$ indicates that the deposit's lateral width or spot radius is smaller than the nozzle throat diameter, and $FR > 1$ means a divergence in the deposition width. The collection efficiency (CE) indicates how many particles have been deposited on the substrate. This is calculated by dividing the number of particles that ended up on the substrate by the total number of particles introduced into the flow. A higher CE with lower FR indicates better performance of the nozzle.

3.1.1. Flow simulation

In the first set of results, the flow field after the nozzle and in front of the impaction plate is discussed, and a comparison is made between the accuracy of different meshes in the calculation of the flow profile when using adaptive mesh refinement. The flow field, including the axial flow

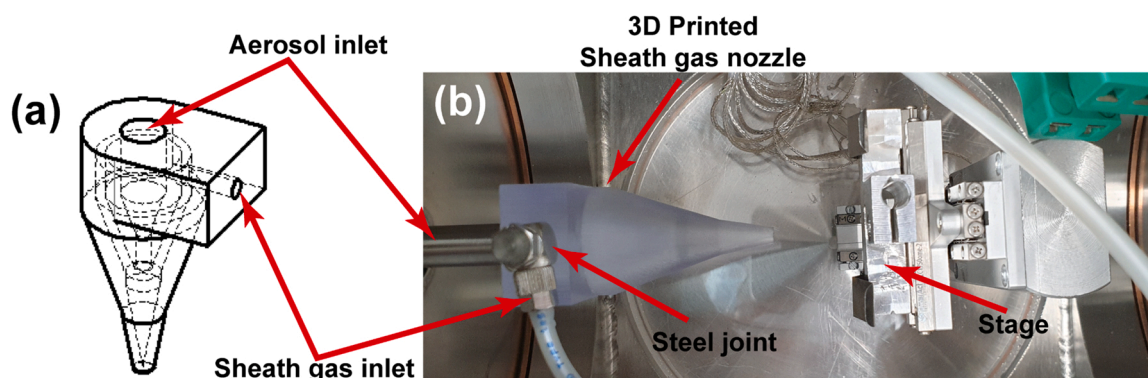


Fig. 3. a) The sheath gas nozzle designed in SolidWorks, b) connection of the 3D printed nozzle with the aerosol and sheath gas inlets in the setup (Fig. S2).

velocity, the radial flow velocity, the pressure gradient in the nozzle throat and in the area between nozzle throat and impaction plate, is shown in Fig. 4 for an outlet pressure (P_d) of 100 Pa and pressure ratio $P_u/P_d=1000$. An imaginary plane, known as a Mach-disk or bow-shock, is formed when high-pressure ratio flows impinge on impaction plates necessitates mesh refinement [48–50]. A coarse mesh was used in the first set of results, and the Mach-disk is not visible. Refining the mesh in the area around the Mach disc results in a clear presentation of the disc, with a very sharp change in axial velocity, radial velocity and pressure. The effect of this plane is more evident for the axial velocity and the pressure; the axial velocity decreases from ~ 450 to ~ 100 m/s, and the pressure increases from ~ 150 to ~ 600 mbar. This abrupt change in velocity and pressure affect the relaxation time and the Stokes number, particularly for smaller particles, lowering their deposition probability. As a result, there are two regions after the nozzle: the first starts at the nozzle throat and continues until the Mach-disk, which is an expansion zone that causes particles to accelerate to higher velocities; the second one starts at the Mach-disk and continues until the impaction plate, which is a stagnation zone that causes particles to decelerate.

3.1.2. Converging nozzle

We first review the simulation results for the converging nozzle (CN). Table S2 summarises the modelled configurations and the value range for each design and operational parameter. The contraction factor (CF) for the CN is ≈ 1 for each modelled situation, i.e., the focusing of particles in the nozzle is due to the decrease in radius only, which is understandable given the considered dominant force (Stokes drag force only). The operational parameters (working distance and downstream pressure) have hardly any effect on the CF; as for the design parameters, the half-angle of the converging section has a more noticeable effect than the nozzle throat diameter but is still negligible. Details of the effects of design and operating parameters on the CF are discussed in the Supplementary Information (Section 5.1.1, Fig. S4-S6).

The effects of design and operating parameters on the focusing ratio (FR) and collection efficiency (CE) of gold nanoparticles for the converging nozzle are shown in Fig. 5. The CE for all parameters (Fig. 5. b, d, f and h) shows that nanoparticles of 5 nm are either not deposited or partially deposited depending on the design and operational parameters; particles of all other sizes are deposited. Fig. 5. a, c, e, and g show

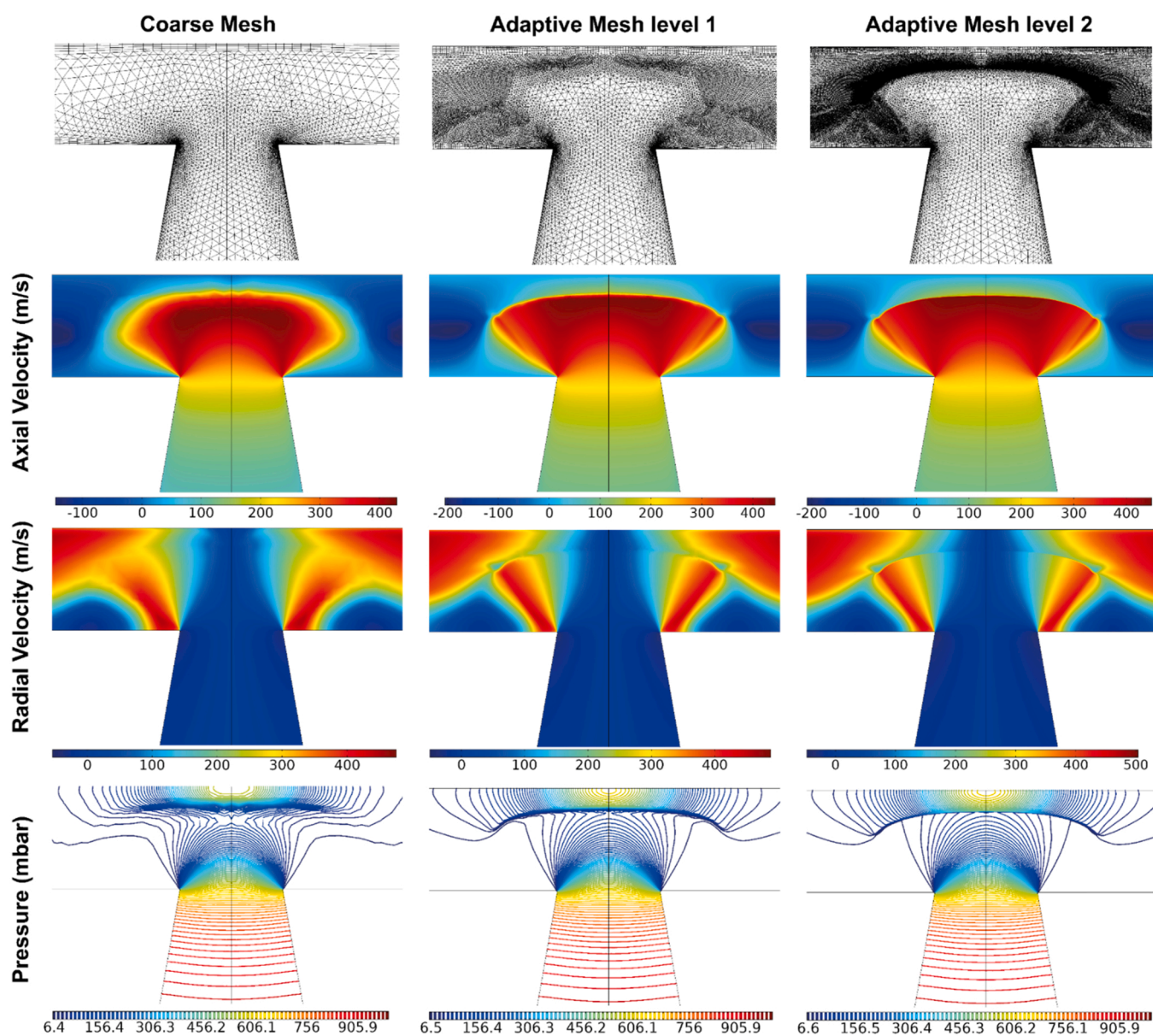


Fig. 4. Effect of meshing on the final result of axial flow velocity, radial velocity, and pressure for coarse, first-level, and second-level mesh refinement. The outlet pressure is set to 100 Pa, the nozzle diameter is 400 μm , and the working distance is 400 μm .

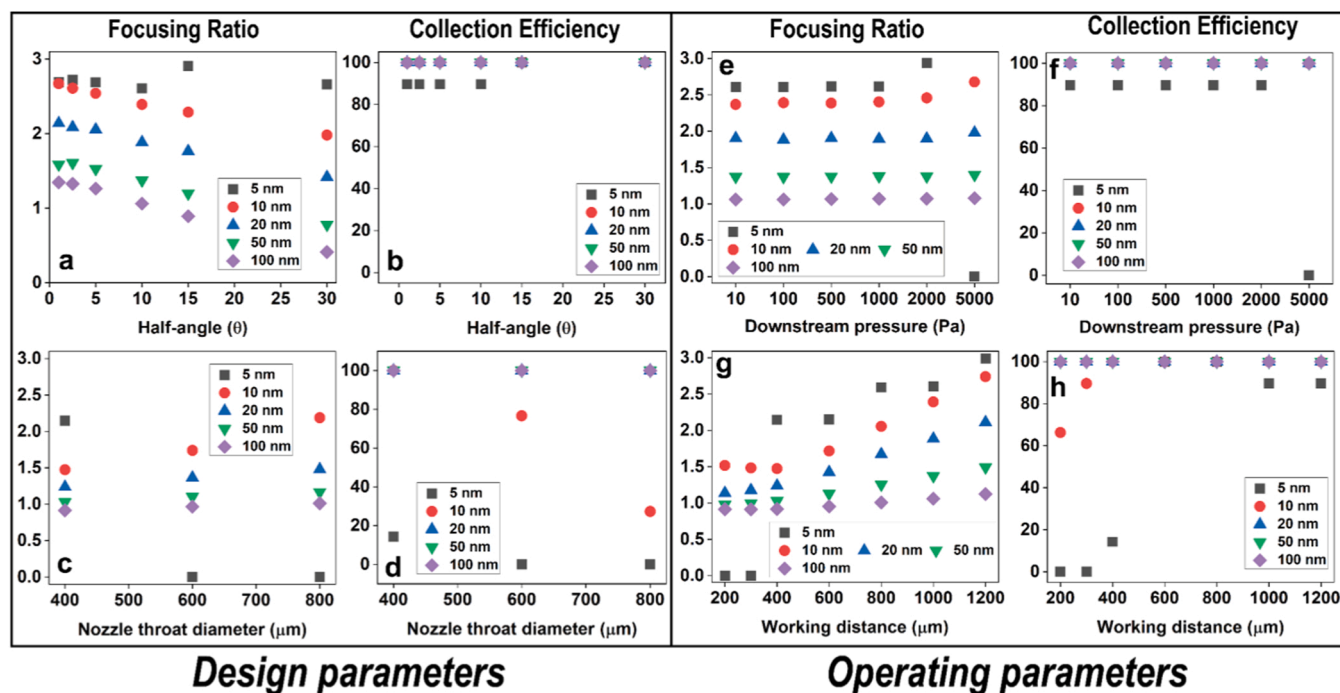


Fig. 5. The focusing ratio and collection efficiency for gold nanoparticles of different sizes in the presence of a CN, varying a, b) the half-angle of the converging nozzle, c, d) the nozzle throat diameter, e, f) the downstream pressure, and g, h) the working distance.

that FR is highly dependent on particle size, with larger particles having a lower FR than smaller ones, implying that higher inertia leads to better particle focusing on the substrate. As the inertia of the particles increases, the Stokes number of the particles increases as well, resulting in the particles' trajectory from the nozzle to the impaction plate being preserved.

Increasing the nozzle half-angle results in a smaller value for FR, and the best FR is achieved with larger particles (Fig. 5.a). For the smallest particles considered (5 nm diameter), the simulation suggests a threshold value for the half-angle to have 100% CE (Fig. 5.b). For the nozzle throat diameter, there is again a threshold value that determines the deposition for the smallest particles (Fig. 5.c), and the effect on FR depends on the particle size (Fig. 5.d), implying that the deposition width is determined by the nozzle throat diameter and has a constant relationship. The downstream pressure has little effect on FR within the chosen value range (Fig. 5.e) and particularly affects the CE for the smallest particles (Fig. 5.f). Increasing the downstream pressure affects the relaxation number of particles through the gas mean free path and the Cunningham slip correction factor (Supplementary information-Section 1: equations (4) and (5)), which mainly affects smaller-sized particles (5 nm). Also, an increase in downstream pressure results in a weaker expansion zone with lower flow velocity, and hence particle velocity, after the nozzle exit, see also Fig. S7. e. When the axial and radial velocity of particles hitting the substrate are considered (Fig. S7), it is clear that smaller particles hit the substrate with a relatively low axial velocity and a high radial velocity, reducing perhaps their deposition probability in reality.

The effect of the nozzle to substrate distance (working distance, WD) on both CE and FR is more complex; see Fig. 5.g and 5.h. There is a threshold value for the WD to guarantee particle deposition, in line with impactor theories (Fig. 5.h) [51]. For larger particle sizes, the FR stays constant with increasing WD, but for smaller particles, FR increases with increasing WD (Fig. 5.g). This can be understood by analysing the flow field after the nozzle exit (Fig. S8). For small WD ($WD/D=0.5$, $WD=200\ \mu\text{m}$), the gas cannot fully expand, causing the gas energy to primarily lead to high radial flow velocity rather than axial velocity, which leads to rejection of particle deposition, particularly for $<10\ \text{nm}$

particles. Fig. S7. g shows that for low WD, 10 nm nanoparticles impinge on the substrate at such low velocity that their chance of deposition is perhaps negligible. Increasing the WD above $300\ \mu\text{m}$ leads to complete gas expansion, and a further increase of WD leads to a larger high-velocity zone before the bow-shock. This increased expansion zone allows particles to accelerate to high velocities and, as a result, high Stokes numbers, enabling them to overcome the deceleration in the stagnation zone so that even very small particles will deposit on the substrate, but on broader regions.

3.1.3. Sheath gas nozzle

Table S3 contains the configuration and specific geometrical and operational details for each study and the range of each parameter to investigate SGN nozzles. Two additional parameters are investigated for this nozzle system: the aerosol nozzle radius and the aerosol flow rate to total flow rate ratio. The computational results for the sheath gas nozzle are depicted and discussed in Supplementary Information, Section 5.1.2, considering the effect of design and operating parameters on the CF (Fig. S9). Unlike the converging nozzle, the CF reaches values above 1, demonstrating the effectiveness of this nozzle in forcing particles towards the centric regions beyond what can be expected from the geometrical convergence. The results show that design parameters of convergence half-angle and inlet nozzle radius or process parameters of downstream pressure and working distance do not affect CF. The most significant insight from Fig. S9 is the effect of aerosol to total flow rate ratio on CF, which shows that the CF is roughly equal to the square root of total flow rate to aerosol flow rate ratio ($\sqrt{\dot{Q}_{\text{Total}}/\dot{Q}_{\text{Aerosol}}}$).

Fig. 6 depicts the effects of design and operation parameters on the FR and CE of (gold) nanoparticles. The inner nozzle radius has a minor effect on the FR and CE (Fig. 6. a and b) and the particles' axial and radial velocities during deposition (Fig. S13. a and b). Increasing the half-angle of the converging section reduces the width of the deposition spot and leads to better focusing (Fig. 6.c) but has no effect on the axial and radial velocities of nanoparticles during deposition (Fig. S13. c and d). It is also clear that the collection efficiency is independent of the half-angle (Fig. 6.d) and is primarily determined by the inertia of the

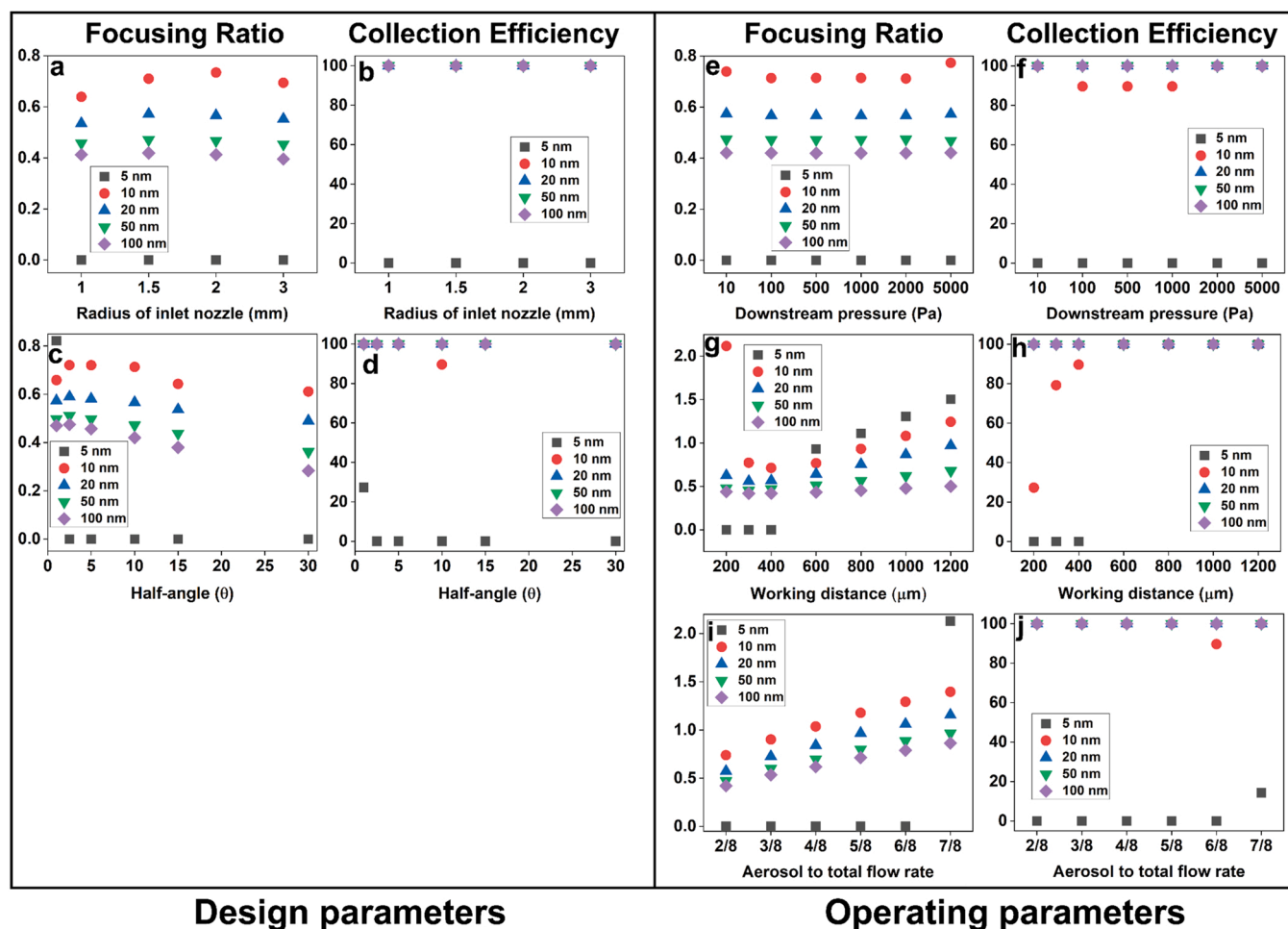


Fig. 6. Focusing ratio and collection efficiency for gold nanoparticles of different sizes for SGN a, b) for Aerosol throat diameter, c, d) for the half-angle of the converging section, e, f) for downstream pressure, g, h) for the distance between nozzle and the impaction plate (working distance), and i, j) for the ratio of aerosol flow rate to the total flow rate.

nanoparticles; thus, low inertia particles have a low deposition probability (5 nm nanoparticles). The FR and the CE are independent of downstream pressure in the chosen range (Fig. 6. e and f); moreover, this parameter has a negligible effect on the axial and radial velocity of the particles during deposition (Fig. S13. e and f). The distance of the nozzle to the substrate (WD) has a significant impact on the FR of nanoparticles (Fig. 6.g). Increasing the WD improves the probability of smaller nanoparticles to be collected (Fig. 6.h) and increases their axial velocity without affecting their radial velocity (Fig. S13. g and h). The ratio of aerosol flow to total flow is the most critical parameter affecting the focusing ratio—the confinement of aerosol flow by sheath gas results in a decrease in nanoparticle deposition width. The further reduction of aerosol flow causes $FR < 1$ (Fig. 6.i), especially for smaller inertia nanoparticles, which was impossible to achieve with a converging nozzle. Fig. 6.j indicates that the flow rate ratio does not affect the CE of particles of different sizes.

In conclusion, sheath gas nozzles are preferable to converging nozzles for the effective trapping of small particles due to: 1) the ability to achieve a narrower line width with a larger nozzle diameter, which is advantageous for both nozzle manufacturing and printed line resolution; 2) better performance in trapping of smaller size nanoparticles; 3) a lower sensitivity to downstream pressure, which allows the system to operate with a less demanding vacuum environment; and 4) a lower sensitivity to design parameters. Higher sheath gas flow rates in an SGN result in better CF for all particle diameter ranges and better FR, resulting in smaller line width. The nozzle throat diameter is the second

most important parameter, as the final deposition feature resolution for both converging and sheath gas nozzles depends on the outer diameter of the nozzle. In order to examine the effect of material density on CF, FR, and CE, the same study was repeated for copper NPs and results are presented in Supplementary information Section 5.2 in Figs. S14–S21. These results show that the density of particles has only a minimal effect on CF for both converging and sheath gas nozzles, but it has a significant effect on both CE and FR. Lower material density results in lower inertia, which has the same effect as smaller size in terms of the overall effect. The model confirms that the line width will be higher, and CE will be lower for lower density nanoparticles compared to similar-sized particles with higher densities.

3.2. Experimental results

This section presents the experimental results for both converging and sheath gas nozzles. We first assess each nozzle's performance in terms of line morphology and dimensions, and then we investigate the effect of operating parameters such as working distance and aerosol flow to total flow rate ratio on the width and thickness of the line printed with each nozzle. Moreover, we investigate the overspray problem in the line, which is caused by the deposition of particles on a broader region with lower density, which decreases the line's resolution and sharpness.

3.2.1. Characterisation of the line printed with CN

Fig. 7.a-f depicts SEM images of a line of gold nanoparticles (AuNPs)

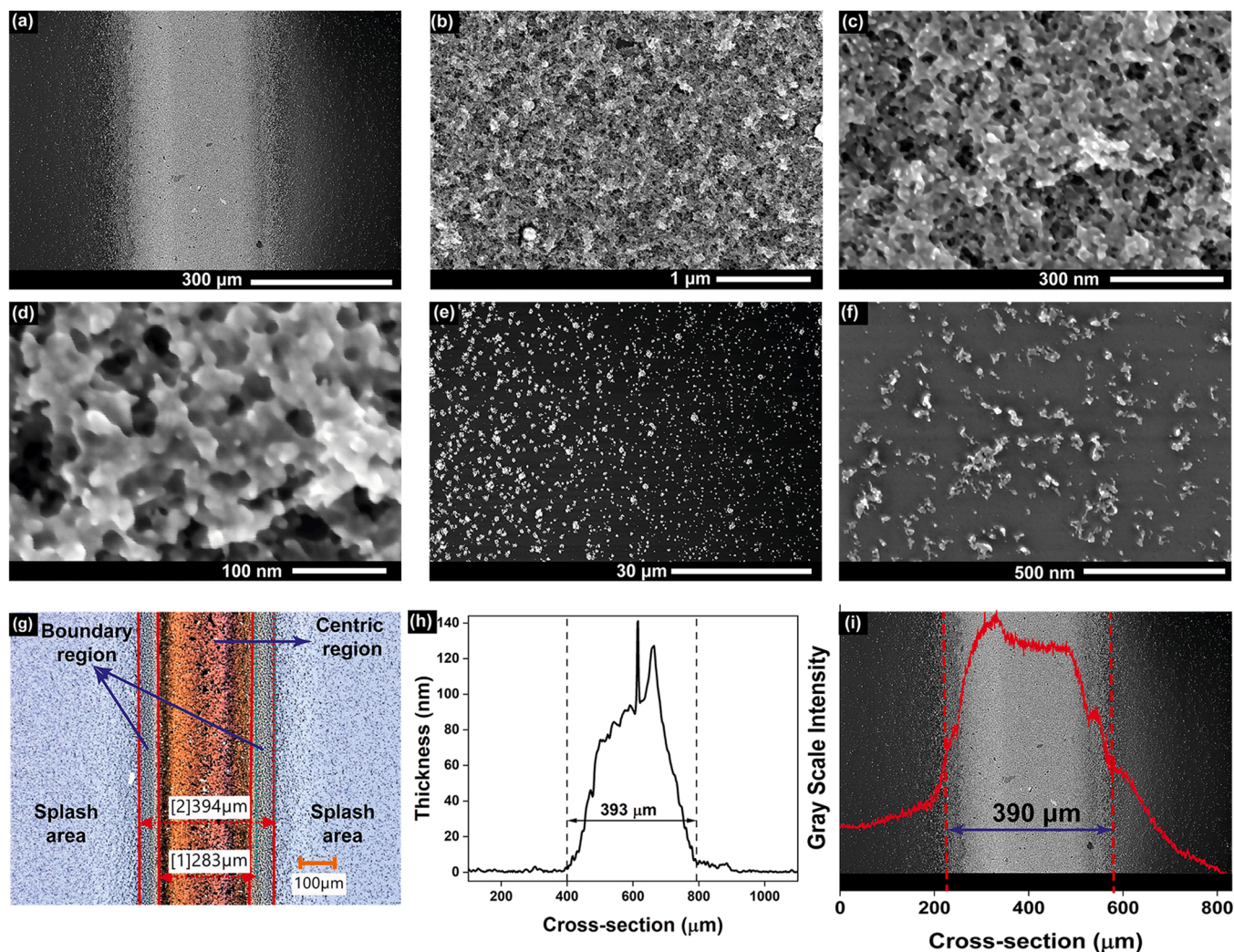


Fig. 7. a) SEM image of a line printed with a CN of 339 μm and WD of 450 μm , b-d) high magnification images of the morphology of the printed line in the centric region, e) SEM image of the boundary and splash area, f) HR-SEM of particles deposited in the splash area, g) optical microscopy image of the line, h) profile of the line measured with white light interferometry, i) SEM image of the line and greyscale intensity diagram of the line.

deposited on a silicon substrate with a converging nozzle (throat diameter of 339 μm) and the typical morphology and density of the AuNPs. Fig. 7.b,c show the morphology of the line in the centric region, which is characterised by the presence of high porosity randomly formed 3D microstructures with nanometric features. A closer examination of the microstructures in Fig. 7.d reveals that they are 3D porous structures formed by a nanometric network of AuNPs. When moving towards the line's outer region, first, we observe a region of the lower density of particles, followed by a splash area with random and low-density deposition of nanoparticles and agglomerates of nanoparticles. Fig. 7.e shows that larger particles are deposited closer to the centre of the line (left side of the image), while further away from the line, smaller particles are deposited, which is consistent with simulation results showing that particles of smaller size deposit over a broader region.

Fig. 7.g shows an optical microscopy image of three regions of the deposited line: 1- the centric region, which features a clear texture and colour and contains dense packing of nanoparticles; 2- the boundary region, which has a different texture but high surface coverage and less dense packing, and 3- the splash zone, which has sparse deposition, and characterised by a low density of particles spread within a broader region, which decreases the resolution. As shown in the image, the width of the centric region is 283 μm , and the width of the line, including the boundary region, is 394 μm . Line width measurements from the optical

microscope and white light interferometry (WLI) are in good agreement (see Fig. 7.h. The splash zone is not evident in the WLI data but is visible in the SEM and optical images (Fig. 7.g,i). This is due to lower coverage in this zone, and the thickness is in the order of noise of the WLI measurement. The greyscale intensity graph for the SEM image of the line in Fig. 7.i was created by integrating the entire image, so the splash zone has a low intensity. When the greyscale data is compared to the WLI results, it is clear that the width estimated using the WLI findings considers the line's boundary but not the splash area.

Fig. S22. a1-d1 illustrates SEM images of the border between the boundary and splash zones of a line printed by a nozzle with a diameter of 339.0 μm and four WDs of L/D equal to 1.18, 1.33, 1.62, and 2.95. The border is clearly visible for larger WDs (Fig. S22. b1-d1) due to differences in the contrast of the two zones caused by differences in either surface coverage or thickness of the deposited layer, and slightly visible for L/D= 1.18 due to a decrease in surface coverage (Fig. S22. a1). Furthermore, the images in Fig. S22.a1-d1 reveal that for lower WDs (1.18 and 1.33) in both the boundary and splash zones, the smaller particles are not deposited because there is a clear contrast between the deposited AuNPs and the black background as the substrate. However, increasing the WD (1.62 and 2.95) results in the deposition of finer nanoparticles, resulting in the formation of a grey background in Fig. S22. c1 and d1. Higher magnification SEM images of Fig. S22. a2-d2

in the splash zone clearly show the presence of finer AuNPs for higher WDs. The same trends were observed in numerical results in Fig. 5.h, indicating that increasing the distance between the substrate and the nozzle increases the probability of depositing finer nanoparticles. The splash zone far from the line's edge shown in Fig. S22. a3-d3, indicating that increasing the WD causes a higher likeliness of trapping finer nanoparticles, in line with modelling results.

3.2.2. Characterisation of the line printed with SGN

Fig. 8 shows high-magnification SEM images of lines printed with an SGN. The AuNPs were deposited on a silicon substrate employing a sheath gas nozzle with an outlet diameter of 248 μm , an aerosol to the total flow rate of 0.31, and a working distance of 250 micrometres. In

Fig. 8.a–c, high magnification SEM images of typical morphology and density of AuNPs in the centric region are shown. The morphology of the lines printed with the SGN is comparable to lines written with the CN.

However, it becomes apparent when comparing the SGN printed lines in Fig. 8.d–f with the CN printed lines in Fig. 7.a and Fig. S22. a1–d1 that the main effect of the SGN is on the line's boundary and splash zone. By comparing the SGN lines' boundary in Fig. 8.g–i with the CN lines in Fig. S22. a1–d1, the splash area is barely visible, and the lines have a distinct edge. When the splash area in Fig. 8.j–l is examined in greater detail, only a very small splash area appears to exist next to the edge of the line, indicating that the particles barely deposit in this area. The splash zone in the SEM images of the CN printed lines (Fig. S22. a1–d1) has a length of more than 40 μm after the boundary region and extends

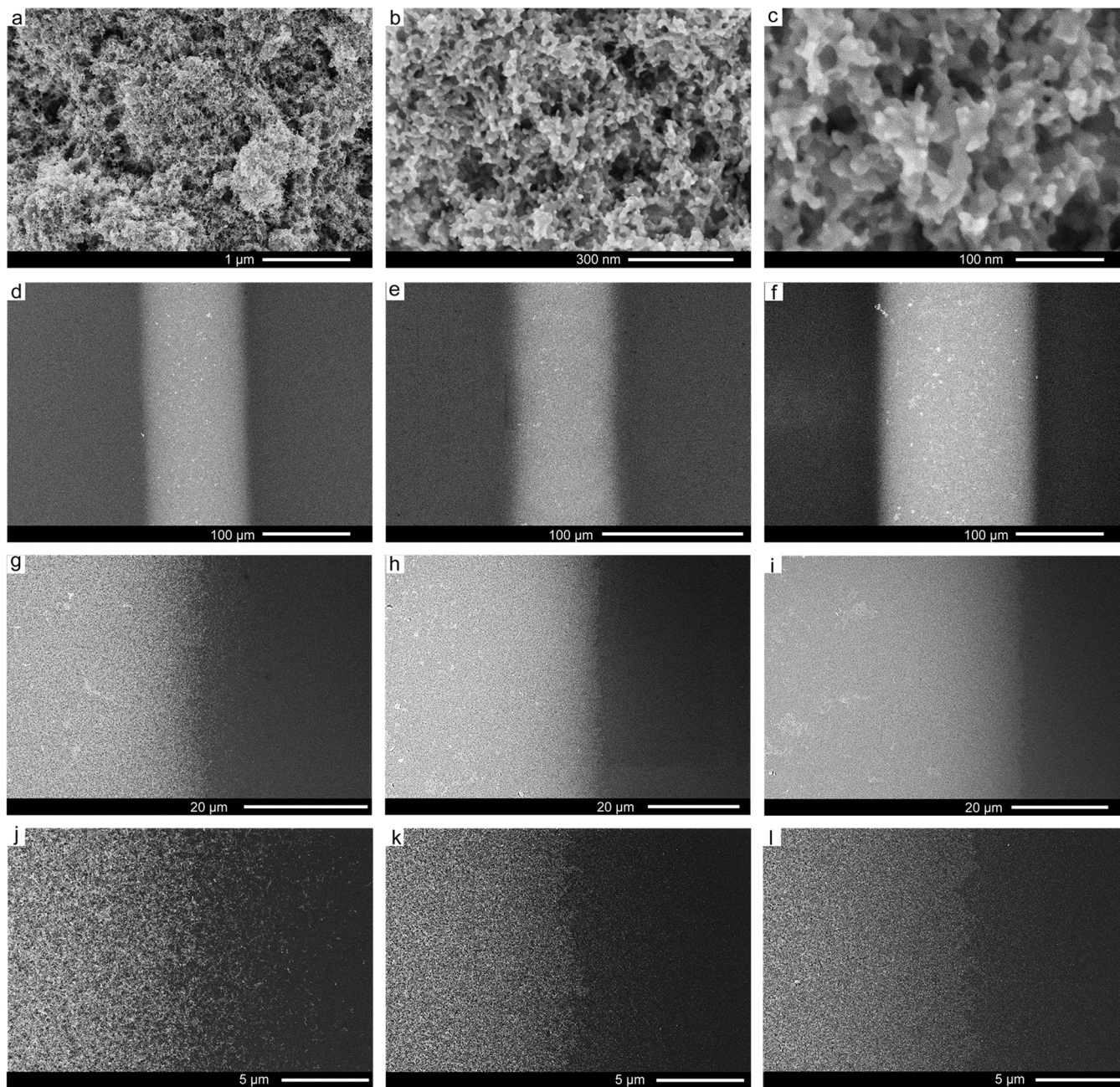


Fig. 8. a–c) high magnification SEM images of the morphology of the centric region of the printed line with an SGN of 248 μm outlet diameter and aerosol to total flow rate (a/T) = 0.31 and WD = 250 μm . The lines and boundaries of the line printed with 248 μm SGN nozzle and process parameters of d) a/T = 0.17 and WD = 700 μm , and boundary and splash area in g) and j), e) a/T = 0.1 and WD = 400 μm , and boundary and splash area in h) and k), f) a/T = 0.31 and WD = 400 μm , and boundary and splash area in i) and l).

to a larger area, whereas the splash zone in the SGN printed lines has a length of only a few micrometres after the boundary region. This demonstrates that utilising SGN improves the sharpness of the printed line, which is crucial when printing lines with a small spacing between them.

3.2.3. Effect of WD on the CN printed line dimensions

Fig. 9.a,b shows how the working distance (WD) affects the thickness and width of the lines printed with three converging nozzles with diameters of 166.5, 238.0, and 339.0 μm respectively and a stage speed of 0.44 m/s. By increasing the WD, the thickness of the lines decreases while the width of the lines increases. This is in agreement with the modelling results (Fig. 5 and Fig. S8). The variation in width increases as the WD increases, as shown in Fig. 9.b; however, these variations are not visible in the optical microscopy images, as shown in Fig. S23. Nonetheless, as the WD increases, the thickness decreases and its amplitude approaches that of noise in the white light interferometry results. As a result, the edge in the boundary is not a defined region, as it appears as a hue in Fig. S23.

Fig. 9.c depicts the thickness as it relates to the normalised working distance to the corresponding nozzle diameters (WD/D). As shown in the graph, for the same WD/D, the thickest line is deposited by the smallest nozzle, and this may be due to variations in the concentration of nanoparticles in the carrier gas. The power of the SAM set up (current=8 mA and voltage=1.1 kV) is constant for all measurements; thus, the amount of material atomised and ablated from the electrodes is constant; however, the argon gas flow rate varies for different nozzles due to stagnation upstream of the nozzle and changes with respect to the nozzle diameters. For nozzles with diameters of 166.5, 238.0, and 339.0 μm , the flow rate of argon is 0.59, 0.99, and 1.39 lpm,

respectively. As a result, lower flow rates result in higher particle concentration and number deposited in the narrower region, resulting in higher thicknesses for smaller diameter nozzles. When comparing the normalised width and normalised working distance to the corresponding nozzle diameters in Fig. 9, it is possible to see that the smallest nozzle has a lower normalised width, but the other two nozzles follow the same trends. One explanation for a narrower line using a smaller nozzle is that the smallest nozzle has a higher degree of agglomeration. The nucleation and growth of primary nanoparticles in the SAM particle generator are symmetrical at an early stage after atomisation and formation of the elemental cloud, which is caused by the high energy of the atoms and results in the formation of spherical polydispersed primary nanoparticles with size distributions less than 20 nm [34,35,52]. Following this stage and energy reduction by both the nucleation-growth mechanisms and the reduction of temperature in the gas flow, the growth mechanism shifts to the agglomeration mechanism. In this mechanism, particles begin to form arbitrary shapes as a result of impact with one another. In addition, as previously stated, the concentration of nanoparticles is higher due to the lower flow rate of argon, which primarily increases the probability of particle interaction and, consequently, the likelihood of agglomeration.

Furthermore, a lower flow rate results in a lower average flow velocity in the connection tube and a long time for particles to travel from the generation site to the deposition chamber compared to higher flow rates. As a result, even with a constant agglomeration rate for all nozzles, longer transportation times result in a different agglomeration size distribution. The minimum width of the lines obtained for a converging nozzle is 168 μm and generated using the nozzle with the smallest diameter (166.5 μm), with an FR of approximately 1. Considering the

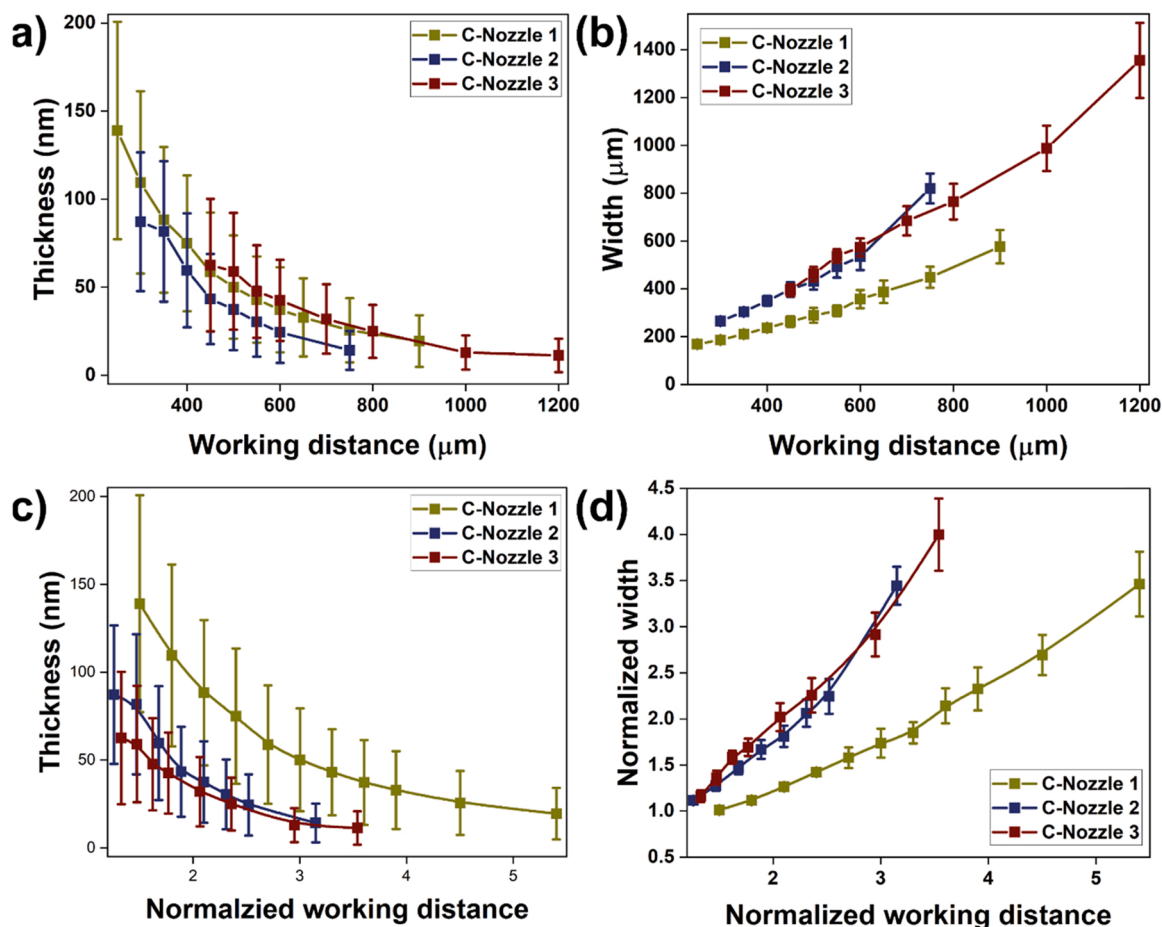


Fig. 9. Effect of working distance on a) thickness and b) width of the AuNPs line printed with three converging nozzles of C-Nozzle 1–3 with a diameter of 166.5, 238 and 339 μm . c) Thickness and d) normalised width to normalised working distance with corresponding nozzle diameter. The stage speed is set to 0.44 mm/s.

numerical results, it is expected that this FR occurred for larger particles distribution of 50–100 nm.

3.2.4. Effect of flow rate ratio and working distance on the SGN printed lines

The aerosol to total flow ratio results for two sheath gas nozzles with exit diameters of 248 and 484 μm , respectively, are summarised in Fig. 10. Using the WLI technique, we measured the width and thickness of lines for 648 cross-sections and three different working distances. The stage speed for deposition of AuNPs with a 248 μm nozzle is 0.11 mm/s, and 0.22 mm/s with a 484 μm nozzle. The dADW flow rate is a function of the nozzle diameter, which influences the concentration of nanoparticles in the stream and, most likely, the particle size distribution due to agglomeration during transportation, as previously stated. Although the outlet diameter of each sheath gas nozzle remains constant throughout the experiment, the aerosol flow rate will change due to changes in the aerosol to total flow ratio, resulting in changes in nanoparticle concentration. A waste channel between the spark discharge generator and the nozzle is employed to maintain a constant nanoparticle concentration. As a result, the total flow rate is 0.42 lpm for a 248 μm nozzle and 1.7 lpm for a 484 μm nozzle. However, it should be noted that the particle generator's power is fixed; as a result, the particle concentration differs between the two nozzle experiments.

As shown in Fig. 10.a-d, the average thickness and width of the deposited line increase with decreasing sheath gas for all working distances. On the other hand, the relationship between the width and thickness and the flow rate ratio is unique for each nozzle, rather than following any general pattern. This could be due to a difference in nanoparticle concentration between the nozzles, with a smaller

diameter nozzle having a higher concentration and, therefore, larger particles sizes due to agglomeration. Fig. 10 shows that lines up to ~ 300 and ~ 600 μm in width were printed using nozzles of 248 and 484 μm in diameter and an aerosol to flow rate of 0.5. With a low aerosol to total flow ratio of 0.17, lines can be produced as narrow as 67 μm . This means that by using an SGN, it is possible to deposit AuNPs in lines with widths equal to approximately 27% of the nozzle throat diameter and at a distance equal to 1.2 times the nozzle throat diameter. Further, the width and thickness of the line are strongly related to the working distance (WD) as they all increase simultaneously due to higher collection efficiency at higher WDs. As shown in Fig. 10, a width of 170 μm , as the narrowest line achieved with a CN, was deposited using a 248 μm SGN and at working distances of 400 and 500 μm while similar line width was printed with a CN of 166.5 μm diameter and a working distance of 200 μm .

4. Conclusion

In this study, we evaluate the performance of dry aerosol direct-writing (dADW) as a simple and solvent-free method for additive manufacturing high-resolution micrometric patterns of < 100 nm-sized nanoparticles through aerodynamic focusing. We investigate, via numerical and experimental approaches, the effect of design and operating parameters on the resulting resolution of sub-100 nm gold nanoparticles lines deposited via a converging nozzle (CN) and sheath gas nozzle (SGN). We assessed three main parameters: the contraction factor (CF), the focusing ratio (FR), and the collection efficiency (CE) to analyse the numerical data. As a result, we discovered that, firstly, CNs are unable to deposit very fine nanoparticles (less than 10 nm) or are only partially

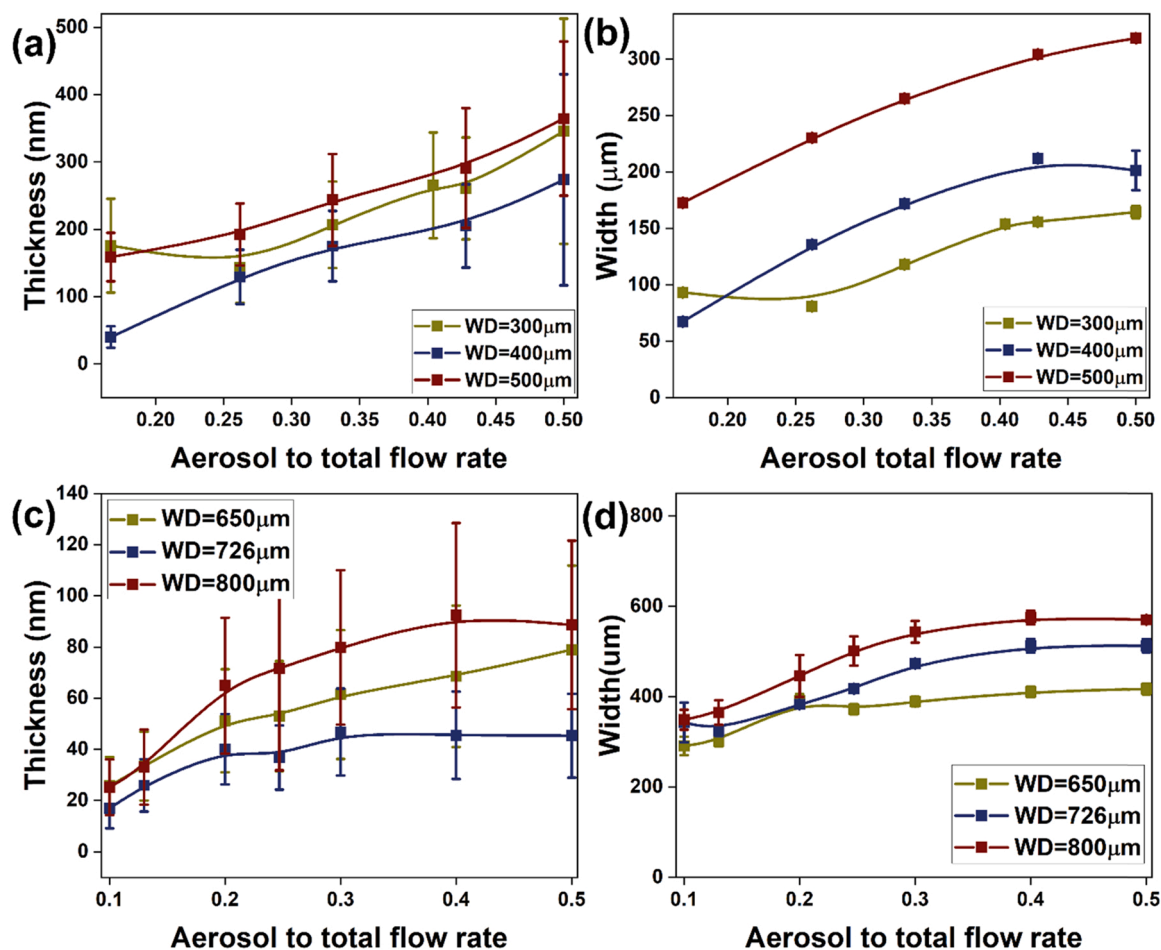


Fig. 10. Effect of aerosol to total flow rate ratio on a, c) thickness, b, d) width for lines printed with nozzles of a, b) 248 μm and c, d) 484 μm diameter.

capable of depositing in a very wide region. Secondly, they are unable to efficiently collimate the particles in the flow and achieve high CF; thirdly, the width of the line is related to both the nozzle diameter and the working distance (WD), and finally are sensitive to the design parameters. This means that when using a WD equal to the diameter of the nozzle, the narrowest line one can expect to print with a CN is in the order of the diameter size of the nozzle throat. Therefore, printing patterns with widths less than 100 μm would necessitate precise nozzle manufacturing and precise nozzle positioning with respect to the substrate. SGNs, on the other hand, firstly are extremely efficient in collimating a beam of particles and achieving high CF due to the presence of a secondary flow, which acts as a virtual tube surrounding the aerosol flow. Secondly, they show very low sensitivity to design parameters for CF and FR, resulting in simplifying the nozzle's design and manufacturing. Thirdly, SGN enables particle deposition in a region smaller than the diameter of the nozzle throat when using a WD equal to the diameter of the nozzle. The combination of low sensitivity to design parameters and the ability to achieve a narrower line while using larger nozzle sizes and greater WDs simplify the design and manufacturing of SGNs.

Although modelling was carried out in order to understand the effect of parameters that we were able to control in the dADW machine or manufacturing of the nozzle, there are a number of variables that were not taken into consideration in the numerical study, which resulted in a difference between the simulation and experimental results. A freeze boundary condition is assumed for the impaction plate in our models, which may differ from reality. In this assumption, particles are considered deposited as soon as they come into contact with the substrate at any impaction velocity, with no consideration given to bouncing of particles from the surface or detachment of particles from the substrate as a result of low interaction between particles and the substrate. Therefore, the particle collection efficiency estimated in simulation is expected to be higher than in experiments. Furthermore, as particles hit the substrate with a lower axial velocity in the outer region of the line, it is reasonable to expect that the line width will be larger in the numerical results. In our modelling, another simplifying assumption is related to the neglect of surface roughness and surface energy and their possible effect on the deposition width and the collection efficiency, which may need to be considered in future studies.

Another source of discrepancy between simulation and experimental data is the assumption of spherical particles in the simulations. While this assumption holds true for primary nanoparticles because their growth is symmetrical, it does not hold true for agglomerated particles, which are formed by the aggregation of several primary nanoparticles resulting in arbitrary shapes and sizes. It is important to note that, as previously stated in the text, the size distribution of particles in the aerosol flow varies for different nozzles due to agglomeration, the effect of variation in the concentration of nanoparticles, and longer transportation time. Finally, manufacturing the nozzle using a stereolithography 3D printer produces a final part composed of layers of 25-micron thickness that are adhered to one another and generate an interior micrometric roughness, which is not considered in the simulation, which may affect the results.

According to the experimental results, lines printed with both CNs and SGNs have a Gaussian cross-section with a varying thickness from 10 s of nanometres to 100 s of nanometres depending on process parameters such as stage velocity and contain randomly formed 3D microstructures with high porosity and nanometric features. The splash area, defined as an outer area with sparse deposition of finer nanoparticles, is the main difference between CN and SGN lines, and its presence reduces the achievable resolution of the line, moreover, reduce the sharpness of the line. CNs have a very large splash area that extends to the width of the line, reducing the CN's performance in both resolutions and collecting NPs in desired regions. The splash area in a line generated using SGNs, on the other hand, is limited to a few micrometres after the boundary, which increases the sharpness of the line. Notably,

the experimental results confirm that increasing WD increases line width, as shown in both SGN and CN modelling.

Furthermore, we test the effect of the aerosol to total flow ratio on the width of the SGN-printed line. The results show that decreasing the aerosol flow rate reduces the width of the line and concentrates the nanoparticles in a region smaller than the nozzle's diameter. The smallest line printed with CNs has a minimum size equal to the nozzle size. Alternatively, the same line width was printed using an SGN with a greater outlet diameter and greater WDs. The narrowest line generated by an SGN was 67 μm , with a nozzle diameter of 248 μm and a WD of 400 μm , i.e., width is about 27% of the nozzle diameter. This demonstrates that dADW can print high-resolution patterns of nanoparticles with width ranging from 67 μm to 600 μm and thickness ranging from 20 nm up to 400 nm. Due to the solvent-free, room temperature and atmospheric pressure, and in-line particle generation, dADW can be utilised to fabricate nanostructured patterns for optical sensors, gas sensors, and interconnects. Moreover, this method enables the generation and deposition of various metal NPs in the form of patterns on a variety of substrates such as paper, silicon and polymer [8,32].

Funding

This project was supported by funding from the Delft University of Technology through the Nano Engineering Research Initiative (NERI, www.tudelft.nl/neri).

CRediT authorship contribution statement

Marcel Tichem: Supervision, Resources, Writing – review & editing, Funding acquisition, Conceptualization. **Angelo Accardo:** Supervision, Writing – review & editing. **Saleh Aghajani:** Conceptualization, Formal analysis, Investigation, Methodology, Validation, Visualization, Writing – original draft.

Declaration of Competing Interest

The authors declare that they have no known competing financial interests or personal relationships that could have appeared to influence the work reported in this paper.

Acknowledgements

The authors would like to thank Dr Ir. R.A.J. (Ron) van Ostayen for a fruitful comment on the finite element section and Patrick van Holst, Gideon Emmaneel, Spiridon van Veldhoven and Rob Lutjeboer for their technical assistance.

Appendix A. Supporting information

Supplementary data associated with this article can be found in the online version at [doi:10.1016/j.addma.2022.102729](https://doi.org/10.1016/j.addma.2022.102729).

References

- [1] S. Xu, W. Tang, D.B. Chase, D.L. Sparks, J.F. Rabolt, A highly sensitive, selective, and reproducible sensor for detection of trace metalloids in the environment, *ACS Appl. Nano Mater.* 1 (2018) 1257–1264, <https://doi.org/10.1021/acsnm.7b00301>.
- [2] Y.Y. Cai, J.G. Liu, L.J. Tauzin, D. Huang, E. Sung, H. Zhang, A. Joplin, W.S. Chang, P. Nordlander, S. Link, Photoluminescence of gold nanorods: purcell effect enhanced emission from hot carriers, *ACS Nano* 12 (2018) 976–985, <https://doi.org/10.1021/acsnano.7b07402>.
- [3] Y. Chen, J. Dong, W. Gao, J. Qi, X. Yan, X. Kong, Enhanced fluorescence effect from complex nanostructure decorated with the native oxide layer, *J. Opt.* 47 (2018) 283–287, <https://doi.org/10.1007/s12596-017-0423-0>.
- [4] N. Kim, M.R. Thomas, M.S. Bergholt, I.J. Pence, H. Seong, P. Charchar, N. Todorova, A. Nagelkerke, A. Belessiotis-Richards, D.J. Payne, A. Gelmi, I. Yarovsky, M.M. Stevens, Surface enhanced Raman scattering artificial nose for high

- dimensionality fingerprinting, *Nanosci. Technol.* (n.d.), <https://doi.org/10.1038/s41467-019-13615-2>.
- [5] J. Xu, Z. Lian, B. Wei, Y. Li, O. Bondarchuk, N. Zhang, Z. Yu, A. Araujo, I. Amorim, Z. Wang, B. Li, L. Liu, Strong electronic coupling between ultrafine iridium-ruthenium nanoclusters and conductive, acid-stable tellurium nanoparticle support for efficient and durable oxygen evolution in acidic and neutral media, *ACS Catal.* 10 (2020) 3571–3579, <https://doi.org/10.1021/ACSCATAL.9B05611>.
- [6] Y. Kotolevich, O. Martynyuk, J.C.G. Ramos, J.E.C. Ortega, R. Vélez, V.M. Rojas, A. A. Tapia, S. Martínez-González, H.J.T. Vázquez, M. Fariás, R. Zanella, A. Pestryakov, N. Bogdanchikova, V.C. Corberán, Nanostructured silica-supported gold: effect of nanoparticle size distribution and electronic state on its catalytic properties in oxidation reactions, *Catal. Today* 366 (2021) 77–86, <https://doi.org/10.1016/j.cattod.2020.08.028>.
- [7] R. Kumar, A. Kumar, N. Verma, V. Khopkar, R. Philip, B. Sahoo, Ni nanoparticles coated with nitrogen-doped carbon for optical limiting applications, *ACS Appl. Nano Mater.* 3 (2020) 8618–8631, <https://doi.org/10.1021/ACSANM.0C01284>.
- [8] S. Aghajani, A. Accardo, M. Tichem, Aerosol direct writing and thermal tuning of copper nanoparticle patterns as surface-enhanced raman scattering sensors, *ACS Appl. Nano Mater.* 3 (2020) 5665–5675, <https://doi.org/10.1021/acsnano.0c00887>.
- [9] Y.-C. Kao, X. Han, Y.H. Lee, H.K. Lee, G.C. Phan-Quang, C.L. Lay, H.Y.F. Sim, V.J. X. Phua, L.S. Ng, C.W. Ku, T.C. Tan, I.Y. Phang, N.S. Tan, X.Y. Ling, Multiplex surface-enhanced raman scattering identification and quantification of urine metabolites in patient samples within 30 min, *ACS Nano* 14 (2020) 2542–2552, <https://doi.org/10.1021/acsnano.0c00515>.
- [10] M. Haghgoo, R. Ansari, M.K. Hassanzadeh-Aghdam, The effect of nanoparticle conglomeration on the overall conductivity of nanocomposites, *Int. J. Eng. Sci.* 157 (2020), 103392, <https://doi.org/10.1016/j.ijengsci.2020.103392>.
- [11] W. Cui, W. Lu, Y. Zhang, G. Lin, T. Wei, L. Jiang, Gold nanoparticle ink suitable for electric-conductive pattern fabrication using in-inkjet printing technology, *Colloids Surf. A Physicochem. Eng. Asp.* 358 (2010) 35–41, <https://doi.org/10.1016/j.colsurfa.2010.01.023>.
- [12] J. Li, L. Liu, D. Zhang, D. Yang, J. Guo, J. Wei, Fabrication of polyaniline/silver nanoparticles/multi-walled carbon nanotubes composites for flexible microelectronic circuits, *Synth. Met.* 192 (2014) 15–22, <https://doi.org/10.1016/j.synthmet.2014.02.026>.
- [13] D. Lau, S. Furman, Fabrication of nanoparticle micro-arrays patterned using direct write laser photoreduction, *Appl. Surf. Sci.* 255 (2008) 2159–2161, <https://doi.org/10.1016/j.apsusc.2008.07.073>.
- [14] M.-H. Chien, M.M. Shawrav, K. Hingerl, P. Taus, M. Schinnerl, H.D. Wanzenboeck, S. Schmid, Analysis of carbon content in direct-write plasmonic Au structures by nanomechanical scanning absorption microscopy, *J. Appl. Phys.* 129 (2021), 063105, <https://doi.org/10.1063/5.0035234>.
- [15] M.R. Lee, H.K. Lee, Y. Yang, C.S.L. Koh, C.L. Lay, Y.H. Lee, I.Y. Phang, X.Y. Ling, Direct metal writing and precise positioning of gold nanoparticles within microfluidic channels for SERS sensing of gaseous analytes, *ACS Appl. Mater. Interfaces* 9 (2017) 39584–39593, <https://doi.org/10.1021/ACSAMI.7B11649>.
- [16] G.Y. Lee, M.S. Kim, H.S. Yoon, J. Yang, J.B. Ihn, S.H. Ahn, Direct printing of strain sensors via nanoparticle printer for the applications to composite structural health monitoring, *Procedia CIRP* 66 (2017) 238–242, <https://doi.org/10.1016/j.procir.2017.03.279>.
- [17] G.-Y. Lee, M.-S. Kim, S.-H. Min, H.-S. Kim, H.-J. Kim, R. Keller, J.-B. Ihn, S.-H. Ahn, Highly sensitive solvent-free silver nanoparticle strain sensors with tunable sensitivity created using an aerodynamically focused nanoparticle printer, *ACS Appl. Mater. Interfaces* 11 (2019) 26421–26432, <https://doi.org/10.1021/ACSAMI.9B00943>.
- [18] C. Novara, F. Petracca, A. Virga, P. Rivolo, S. Ferrero, A. Chiolerio, F. Geobaldo, S. Porro, F. Giorgis, SERS active silver nanoparticles synthesized by inkjet printing on mesoporous silicon, *Nanoscale Res. Lett.* 9 (2014) 1–7, <https://doi.org/10.1186/1556-276X-9-527>.
- [19] J.G. Korvink, P.J. Smith, D.Y. Shin, Inkjet-based micromanufacturing, 2012. <https://doi.org/10.1002/9783527647101>.
- [20] Z.P. Yin, Y.A. Huang, N.B. Bu, X.M. Wang, Y.L. Xiong, Inkjet printing for flexible electronics: materials, processes and equipments, *Chin. Sci. Bull.* 55 (2010) 3383–3407, <https://doi.org/10.1007/s11434-010-3251-y>.
- [21] D. Deng, Y. Jin, Y. Cheng, T. Qi, F. Xiao, Copper nanoparticles: aqueous phase synthesis and conductive films fabrication at low sintering temperature, *ACS Appl. Mater. Interfaces* 5 (2013) 3839–3846, <https://doi.org/10.1021/am400480k>.
- [22] A. Mahajan, C.D. Frisbie, L.F. Francis, C. Daniel Frisbie, L.F. Francis, Optimization of aerosol jet printing for high-resolution, high-aspect ratio silver lines, *ACS Appl. Mater. Interfaces* 5 (2013) 4856–4864, <https://doi.org/10.1021/am400606y>.
- [23] E.B. Secor, Principles of aerosol jet printing, *Flex. Print. Electron.* 3 (2018), 035002, <https://doi.org/10.1088/2058-8585/aae28>.
- [24] R. Salary, J.P. Lombardi, M. Samie Tootooni, R. Donovan, P.K. Rao, P. Borgesen, M.D. Poliks, Computational fluid dynamics modeling and online monitoring of aerosol jet printing process, *J. Manuf. Sci. Eng. Trans. ASME* (2017), <https://doi.org/10.1115/1.4034591>.
- [25] D.R. Hines, Y. Gu, A.A. Martin, P. Li, J. Fleischer, A. Clough-Paez, G. Stackhouse, A. Dasgupta, S. Das, Considerations of aerosol-jet printing for the fabrication of printed hybrid electronic circuits, *Addit. Manuf.* 47 (2021), 102325, <https://doi.org/10.1016/j.addma.2021.102325>.
- [26] G. Chen, Y. Gu, H. Tsang, D.R. Hines, S. Das, The effect of droplet sizes on overspray in aerosol-jet printing, *Adv. Eng. Mater.* 20 (2018), 1701084, <https://doi.org/10.1002/ADEM.201701084>.
- [27] A. Kamyshny, S. Magdassi, *Inkjet-Based Micromanufacturing*, Wiley-VCH, 2012, pp. 173–189, <https://doi.org/10.1002/9783527647101.ch12>.
- [28] S.V. Klinkov, V.F. Kosarev, M. Rein, Cold spray deposition: significance of particle impact phenomena, *Aerosp. Sci. Technol.* 9 (2005) 582–591, <https://doi.org/10.1016/j.ast.2005.03.005>.
- [29] S. Bagherifard, A. Heydari Astaraee, M. Locati, A. Nawaz, S. Monti, J. Kondás, R. Singh, M. Guagliano, Design and analysis of additive manufactured bimodal structures obtained by cold spray deposition, *Addit. Manuf.* 33 (2020), 101131, <https://doi.org/10.1016/j.addma.2020.101131>.
- [30] J. Akedo, Room temperature impact consolidation (RTIC) of fine ceramic powder by aerosol deposition method and applications to microdevices, *J. Therm. Spray Technol.* 17 (2008) 181–198, <https://doi.org/10.1007/S11666-008-9163-7>.
- [31] G.-Y. Lee, J.-I. Park, C.-S. Kim, H.-S. Yoon, J. Yang, S.-H. Ahn, W.E. Boeing, Aerodynamically focused nanoparticle (AFN) printing: novel direct printing technique of solvent-free and inorganic nanoparticles, *ACS Appl. Mater. Interfaces* 6 (2014) 13–71, <https://doi.org/10.1021/am504304g>.
- [32] S. Aghajani, A. Accardo, M. Tichem, Tunable photoluminescence and SERS behaviour of additively manufactured Au nanoparticle patterns, *RSC Adv.* 11 (2021) 16849–16859, <https://doi.org/10.1039/D1RA02266K>.
- [33] N.S. Tabrizi, M. Ullmann, V.A. Vons, U. Lafont, A. Schmidt-Ott, Generation of nanoparticles by spark discharge, *J. Nanopart. Res.* 11 (2009) 315–332, <https://doi.org/10.1007/s11051-008-9407-y>.
- [34] N.S. Tabrizi, Q. Xu, N.M. van der Pers, U. Lafont, A. Schmidt-Ott, Synthesis of mixed metallic nanoparticles by spark discharge, *J. Nanopart. Res.* 11 (2009) 1209–1218, <https://doi.org/10.1007/s11051-008-9568-8>.
- [35] N.S. Tabrizi, Q. Xu, N.M. van der Pers, A. Schmidt-Ott, Generation of mixed metallic nanoparticles from immiscible metals by spark discharge, *J. Nanopart. Res.* 12 (2010) 247–259, <https://doi.org/10.1007/s11051-009-9603-4>.
- [36] D.L. Schulz, J.M. Hoey, D. Thompson, O.F. Swenson, S. Han, J. Lovaasen, X. Dai, C. Braun, K. Keller, I.S. Akhatov, Collimated aerosol beam deposition: Sub 5- μ m resolution of printed actives and passives, in: *Proc. Acad. Track 2008 Flex. Electron. Displays - Conf. Exhib. FLEX*, 2008. <https://doi.org/10.1109/FEDC.2008.4483871>.
- [37] D.L. Roberts, J.P. Mitchell, The effect of nonideal cascade impactor stage collection efficiency curves on the interpretation of the size of inhaler-generated aerosols, *AAPS PharmSciTech* 14 (2013) 497–510, <https://doi.org/10.1208/s12249-013-9936-2>.
- [38] F. Di Fonzo, A. Gidwani, M.H. Fan, D. Neumann, D.I. Iordanoglou, J.V. Heberlein, P.H. McMurry, S.L. Girshick, N. Tymiak, W.W. Gerberich, N.P. Rao, Focused nanoparticle-beam deposition of patterned microstructures, *Appl. Phys. Lett.* 77 (2000) 910–912, <https://doi.org/10.1063/1.3306638>.
- [39] I.S. Akhatov, J.M. Hoey, O.F. Swenson, D.L. Schulz, Aerosol focusing in micro-capillaries: theory and experiment, *J. Aerosol Sci.* 39 (2008) 691–709, <https://doi.org/10.1016/j.jaerosci.2008.04.004>.
- [40] X. Wang, F.E. Krus, P.H. McMurry, Aerodynamic focusing of nanoparticles: I. Guidelines for designing aerodynamic lenses for nanoparticles, *Aerosol Sci. Technol.* 39 (2005) 611–623, <https://doi.org/10.1080/02786820500181901>.
- [41] R. Streubel, M.B. Wilms, C. Doñate-Buendía, A. Weisheit, S. Barcikowski, J. H. Schleifenbaum, B. Göcke, Depositing laser-generated nanoparticles on powders for additive manufacturing of oxide dispersed strengthened alloy parts via laser metal deposition, *Jpn. J. Appl. Phys.* 57 (2018), 040310, <https://doi.org/10.7567/JJAP.57.040310>.
- [42] S. Opiolka, F. Schmidt, H. Fissan, Combined effects of electrophoresis and thermophoresis on particle deposition onto flat surfaces, *J. Aerosol Sci.* 25 (1994) 665–671, [https://doi.org/10.1016/0021-8502\(94\)90007-8](https://doi.org/10.1016/0021-8502(94)90007-8).
- [43] E. Tabesh, H.R. Salimijazi, M. Kharaziha, M. Mahmoudi, M. Hejazi, Development of an in-situ chitosan-copper nanoparticle coating by electrophoretic deposition, *Surf. Coat. Technol.* 364 (2019) 239–247, <https://doi.org/10.1016/j.surfcoat.2019.02.040>.
- [44] R. Mei, An approximate expression for the shear lift force on a spherical particle at finite reynolds number, *Int. J. Multiph. Flow.* 18 (1992) 145–147, [https://doi.org/10.1016/0301-9322\(92\)90012-6](https://doi.org/10.1016/0301-9322(92)90012-6).
- [45] A. Mahajan, C. Daniel Frisbie, L.F. Francis, Optimization of aerosol jet printing for high-resolution, High-Asp. Ratio Silver Lines (2013), <https://doi.org/10.1021/am400606y>.
- [46] J.Q. Feng, A computational study of particle deposition patterns from a circular laminar jet, *J. Appl. Fluid Mech.* 10 (2017) 1001–1012, <https://doi.org/10.18869/acadpub.jafm.73.241.27233>.
- [47] COMSOL, COMSOL Multiphysics® v. 5.5. www.comsol.com. COMSOL AB, Stockholm, Sweden, (2018).
- [48] Q. Li, Y. LYU, T. PAN, D. LI, H. LU, Y. GONG, Development of a coupled supersonic inlet-fan Navier–Stokes simulation method, *Chin. J. Aeronaut.* 31 (2018) 237–246, <https://doi.org/10.1016/j.cja.2017.11.011>.
- [49] P. Biswas, C. Plagan, C. Plagan, High-velocity inertial impactors, *Environ. Sci. Technol.* 18 (1984), <https://doi.org/10.1021/es00126a009>.
- [50] O. Abouali, G. Ahmadi, A model for supersonic and hypersonic impactors for nanoparticles, *J. Nanopart. Res.* 7 (2005) 75–88, <https://doi.org/10.1007/s11051-004-7910-3>.
- [51] W.C. Hinds, Aerosol technology, *J. Chem. Inf. Model.* 53 (2019) 1689–1699, <https://doi.org/10.1017/CBO9781107415324.004>.
- [52] C. Roth, G.A. Ferron, E. Karg, B. Lentner, G. Schumann, S. Takenaka, J. Heyder, Generation of ultrafine particles by spark discharging, *Aerosol Sci. Technol.* 38 (2004) 228–235, <https://doi.org/10.1080/02786820490247632>.